Volume 1 | Number 1 | Jan 2013 | Pages 1–100

Journal of
Materials Chemistry A

Materials for energy and sustainability
www.rsc.org/materialsA

Li⁺

ROYAL SOCIETY
OF CHEMISTRY

ROYAL SOCIETY
OF CHEMISTRY

www.rsc.org/materialsA

Journal of Materials Chemistry A

ARTICLE

Ultrathin Porous Co_3O_4 Nanoplates as Highly Efficient Oxygen Evolution Catalysts

Xuemei Zhou,[a] Zhaoming Xia,[a] Zhinmin Tian,[a] Yuanyuan Ma,*[a,b] Yongquan Qu*[a, b]

Oxygen evolution reaction (OER) catalysts are of central importance for electrocatalytic/photocatalytic water oxidation and fuel generation. Here we report a new type of ultrathin porous Co_3O_4 nanoplates as highly efficient OER catalysts. The porous Co_3O_4 nanoplates annealed at 250 °C can be readily synthesized in quantities with a large surface area of 160.9 m^2/g, a very small crystalline size of ~3.0 nm, and a thin thickness of ~10 nm. Large surface area provides more surface active sites for OER. The structural features of the porous nanoplates significantly enrich the amount of the surface abundant catalytic sites, provide more active edge and corner cobalt species with low coordination numbers, and subsequently enhance their OER activity. Meanwhile, the thin thickness facilitates the efficient diffusion of the chemicals and the escape of the generated O_2 within the electrode. Given all together, the porous Co_3O_4 nanoplates annealed at 250 °C deliver a high OER activity with an overpotential as low as 258 mV at 1 mA/cm^2, a turnover frequency of 0.0042 s^{-1} (low bound), a Tafel slope of 71 mV/dec in 1.0 M KOH solution and an excellent electrochemical stability.

Introduction

Photo and/or electrochemical water splitting is considered as a promising pathway to a clean and sustainable energy resource — hydrogen.[1-7] Compared to the reduction half-reaction for H_2 generation, the oxygen evolution reaction (OER) involves a four-electron process and is more challenging due to the slow kinetics, the high over-potentials and the low catalytic stability of catalysts.[1-8] Ir- and Ru- based catalysts show effective OER catalytic activities in an aqueous media.[9-12] However, the practical utilizations of Ir- and Ru- materials are limited by their scarce availability and high cost.[13-15] Therefore, there is considerable interest in exploring economical and efficient substitutes composed of earth abundant elements, e.g. cobalt,[13, 16-23] nickel,[22, 24-26] iron[22, 27, 28] and manganese,[22, 29, 30] as the potential alternative OER catalysts.

Inspired by the recent report of Co-Pi electrocatalysts with a high OER activity, much attention has been given to cobalt based materials for water oxidation.[20] In situ X-ray absorption studies indicated that the high OER activities of Co-Pi catalysts could be attributed to the existence of Co_4O_4 cubane in the catalysts.[31] Co_3O_4 has a typical spinel structure, in which Co^{2+} locates at tetrahedral sites and Co^{3+} occupies octahedral sites. The Co_4O_4 cubane formed by octahedral cobalt and oxygen atoms indicates that Co_3O_4 has the potential as the OER catalyst.[32, 33] Previous studies have verified that

the OER activities of Co_3O_4 nanostructures are strongly correlated with their available surface areas.[16] Hence, various strategies have been designed to synthesize Co_3O_4 catalysts with large surface area and small crystalline size. However, the charge transfer of small Co_3O_4 nanoparticles with a large surface area is insufficient due to the existence of a large number of grain boundaries.[16, 34] One approach to solve the charge transfer of small nanoparticles is to synthesize porous Co_3O_4 nanostructures, which preserve the features of large surface area and small crystalline size and reduce the amount of grain boundaries.[16, 34] Another strategy is to maintain small size of Co_3O_4 and enhance charge transfer by dispersing small Co_3O_4 nanostructures on various conductive supports, e.g. Au,[34] Ni foam,[16] multi-wall carbon nanotubes[26, 35] and graphene.[36] Their electrochemical activities clearly demonstrate the promise of Co_3O_4 and their hybrids as efficient and robust OER catalysts. However, most methods reported to date involve time-consuming or complex synthetic procedures. For example, the synthesis of ordered mesoporous Co_3O_4 by a typical hard template method requires multiple steps including: synthesis of template, grafting of cobalt sources, formation of cobalt oxides and removal of template.

Herein, we report a facile method combining wet chemistry and high temperature anneal for scalable synthesis of porous

Co_3O_4 nanoplates. We show that the surface area, pore size, pore density and crystalline size of the resulting porous nanoplates can be easily tailored by the annealing temperatures. The small crystalline of Co_3O_4 is found to be critical to improve the catalytic activity of catalysts in terms of turnover frequency by delivering the abundant amount of the active surface sites with low coordination numbers. The contiguous framework of ultrathin (~ 10 nm) porous nanoplates not only ensures efficient charge transfer by reducing the number of grain boundary but also allow easy escape of generated O_2 and rapid recovery of surface catalytic sites. Moreover, our study clearly demonstrates the higher catalytic activity of the surface active centers is originated from their small crystalline size, which is ignored in the previous studies for Co-based OER catalysts. The porous Co_3O_4 nanoplates annealed at 250 °C exhibit the largest surface area (160.9 m^2/g) and the smallest crystalline size (~ 3 nm), which deliver a high catalytic activity for water oxidation reactions

Experimental

All chemicals are commercially available and used without further purification. NaOH (99%), $Co(NO_3)_2 \cdot 6H_2O$ (98%) and tetraethyl orthosilicate (99%) were purchased from Alfa Aesar.

Synthesis of β-Co(OH)$_2$ and porous Co$_3$O$_4$ nanoplates.

β-Co(OH)$_2$ nanoplates were synthesized by a modified wet chemical process.[37] In a typical synthesis, NaOH (0.16 mol) was dissolved in 35 mL of Milli-Q water (18.2 MΩ $\cdot$ cm) under vigorous magnetic stirring at room temperature. $Co(NO_3)_2 \cdot 6H_2O$ aqueous solution (5mL, 4.0 M) was slowly injected into the NaOH aqueous solution within 5 minutes. After aging for 30 min under continuous stirring, the mixture was transferred into a Pyrex bottle and placed into an electric oven at 100 °C. After 12 hr reaction, the solution was cooled down to room temperature naturally overnight. The products were filtered, washed thoroughly with water and absolute ethanol for three times, and dried at 60 °C overnight. The porous Co_3O_4 nanoplates were prepared by calcining β-Co(OH)$_2$ nanoplates in air for 3 hours at various temperatures with a ramp rate of 1 °C /min. Subsequently, the porous nanostructures were obtained after cooling down to room temperature naturally.

Preparation of ordered mesoporous Co$_3$O$_4$ nanostructures using KIT-6 as hard templates.

Ordered mesoporous KIT-6 was prepared according to previous method.[23,34] Briefly, 13.5 g of surfactant (Pluronic 123, EO20PO70EO20) was dissolved in a mixture of 487.5 g of Milli-Q water and 26.1 g of concentrated HCl (37%). 13.5 g of *n*-butanol was added to the homogenous solution at 35 °C. After stirring the solution for 1 h, 29 g of tetraethyl orthosilicate (TEOS) was quickly added into the solution. The mixture was stirred at 35 °C for 24 h and then maintained at the same temperature for another 24 h under the static conditions. The solid product was filtered without washing, dried at 90 °C overnight, and then calcined at 550 °C for 6 h with a ramp rate of 1 °C/min.

Ordered mesoporous Co_3O_4 nanostructures were prepared by using KIT-6 as the hard template. In brief, 0.2 g of KIT-6 was dispersed in 5 mL of 0.8 M $Co(NO_3)_2 \cdot 6H_2O$ in ethanol. The mixture was stirred for 1 h at room temperature and dried at 60 °C. The obtained powder was calcined at 350 °C for 4 h with a ramp rate of 1 °C/min. Finally, the silica template was removed by dispersing 50 mg of the products in 10 mL of 2 M NaOH solution for 6 hours. The etched samples were centrifuged off, washed thoroughly with water, and dried at 60 °C overnight.

Characterization

The surface area and pore size were measured by nitrogen physisorption (Micromeritics, ASAP 2020 HD88) based on the Brunauer-Emmet- Teller (BET) method. The phase evolution of as-synthesized nanostructures was monitored by powder X-ray diffraction (XRD). The XRD patterns with diffraction intensity versus 2θ were recorded in a Shimadzu X-ray diffractometer (Model 6000) using Cu Kα radiation. Thermogravimetric analysis (TGA) of as-synthesized samples were carried out Mettler Toledo, STAR^e at a heating rate of 5 °C $\cdot$ min^{-1} from room temperature to 800 °C in air. X-ray photoelectron spectra (XPS) were acquired on a Thermo Electron Model K-Alpha with Al Kα as the excitation source. Scanning electron microscopy (SEM) was performed on Hatchie Su-8010 scanning electron microscope. Transmission electron microscopy (TEM) studies were conducted on a Hatchie HT-7700 field-emission transmission electron microscope with an accelerating voltage of 120 kV.

Electrochemical Measurements

Electrocatalytic activities including linear sweep voltammograms (LSV) and chronoamperometry were measured on CHI 660D electrochemistry workstation (CH Instrument, Shanghai, China) with a standard three electrode system in KOH aqueous solutions at various concentrations of 0.01 M, 0.1 M and 1.0 M. The counter electrode was platinum wire and the reference electrode was standard Ag/AgCl (3 M KCl). The catalyst with a loading of 0.56 mg $\cdot$ cm^{-2} on indium tin oxide (ITO) surface was used as the working electrode. The scanning rate for LSV measurements was 50 mV $\cdot$ s^{-1}. Rotating-disk electrode voltammograms were obtained with a scan rate of 10 mV $\cdot$ s^{-1}. Electrochemical impedance spectroscopy (EIS) was performed on the AUTOLAB PGSTAT204 electrochemistry workstation in the frequency range from 0.01 Hz to 100 KHz at an open circuit potential, with 10 mV as the amplitude potential.

Results and discussion

Characterization of β-Co(OH)$_2$ nanoplates

β-Co(OH)$_2$ nanoplates were synthesized by a modified solution process at 100 °C for 12 hrs.[37] Microstructures of the as-prepared products are examined by TEM and SEM. The nanostructures display a near hexagonal plate morphology (Fig.
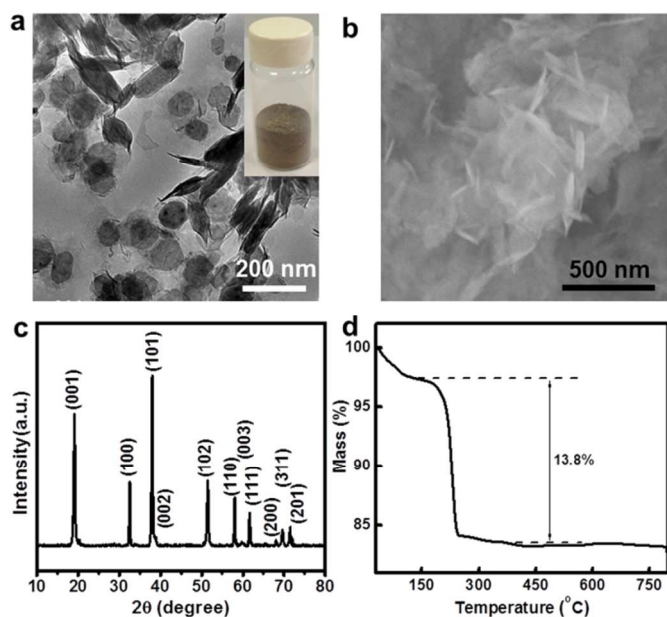
Fig. 1 Characterization of β-Co(OH)$_2$ nanoplates. (a) A typical TEM image. Inset is the photography of the nanoplates obtained from 1.6 L reaction solution. (b) A typical SEM image. (c) XRD pattern. (d) TGA curve in air with a temperature ramp rate of 5 °C/min.

1a). The length of the nanoplate diagonal has a wide distribution from 50 to 200 nm. The thickness of the nanoplates is ∼ 10 nm measured from the vertically aligned nanoplates (Fig. 1b and Fig. S1). XRD studies clearly indicate β-Co(OH)$_2$ phase (JCPDS No. 30-0443) of the as-synthesized nanoplates (Fig. 1c). A small XRD peak at 65 ° may be attributed to the CoO(OH) phase. Notably, the synthesis of β-Co(OH)$_2$ nanoplates (yield, 7.36 g) is scalable as evidenced in the photography (inset Fig. 1a), which was obtained from 1.6 L reaction solution with a yield of about 99%.

The thermal behavior of β-Co(OH)$_2$ nanoplates was investigated by TGA (Fig. 1d). The initial weight loss of the nanoplates up to 120 °C can be ascribed to the desorption of physisorbed and/or trapped water molecules. With increasing the temperature, a sharp weight loss was observed at 210 °C. When the temperature was above 250 °C, the weight variation became negligible. The actual weight loss of the β-Co(OH)$_2$ nanoplates derived from the TGA curve is 13.8%, which is very consistent with the theoretical value (13.6%) for converting Co(OH)$_2$ into Co$_3$O$_4$.

Characterization of porous Co$_3$O$_4$ nanoplates

Hence, β-Co(OH)$_2$ nanoplates were annealed at various temperatures and the resulted products were denoted as Co$_3$O$_4$-x, where x represents the annealing temperature and the synthetic reaction equations (1) are listed the following. Fig. 2 shows the morphologies of the products after heat treatment and their XRD spectra. It was found that β-Co(OH)$_2$ was completely converted into Co$_3$O$_4$ after 250 °C treatments in air (equation 1) for 3 hrs, consistent with TGA results. TEM images (Fig. 2a-2d) reveal that the shape of the nanostructures with an annealing temperature below 500 °C was well
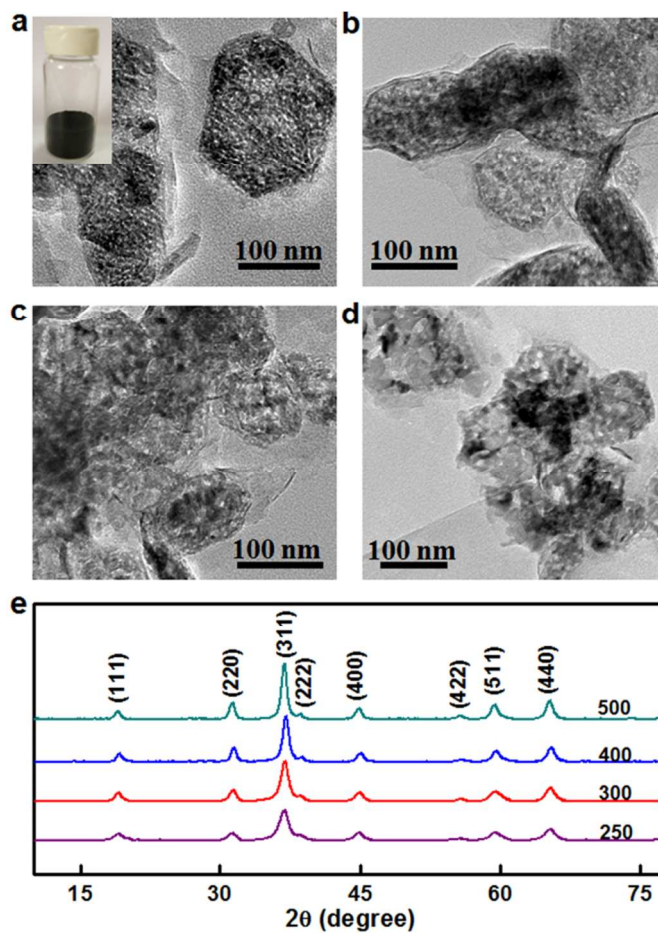
Fig. 2 Structural characterization of porous Co$_3$O$_4$ nanoplates. TEM images of porous Co$_3$O$_4$ nanoplates after thermal treatment (a) 250 °C, (b) 300 °C, (c) 400 °C, and (d) 500 °C. (e) XRD patterns of porous nanoplates show a spinel Co$_3$O$_4$ phase for all products. Inset is the photography of Co$_3$O$_4$-250 obtained from β-Co(OH)$_2$ nanoplates shown in inset of Fig. 1a.

preserved as near hexagonal one. When the annealing temperature was above 600 °C, the collapsed nanostructures were observed (Fig. S2). The XRD pattern of all annealed samples (Fig. 2e) can be assigned to the spinel Co$_3$O$_4$ (JCPDS No.42-1467).

$$6Co^{2+} +12\ OH^- \xrightarrow{Hydrothermal} 6Co(OH)_2 +O_2 \xrightarrow[In\ air]{Annealing} 2Co_3O_4 +6H_2O \quad (1)$$
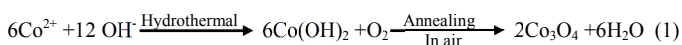
To interrogate the electronic structure of the as-prepared surface, we measured the XPS spectrum of Co$_3$O$_4$-250. All the spectra were referenced to the aliphatic carbon at binding energy (BE) of 284.5 eV. As given in Fig. S3a, it can be seen clearly that the Co(OH)$_2$ and HFC-250 contain the elements of O 1s and Co 2p. High-resolution Co$_{2p}$ spectrum (Fig. S3b) show spin-orbit splitting into 2p$_{1/2}$ and 2p$_{3/2}$ components. The peaks of Co 2p$_{3/2}$ are at 781.1 eV and 780.7 eV for Co(OH)$_2$ and Co$_3$O$_4$-250, respectively. The slight decrease in binding energy for the annealed samples indicates the formation of Co$_3$O$_4$, which is consistent with previous reports.[38, 39]

More importantly, the porous structures after annealing at various temperatures can be clearly seen from TEM images

Table 1. Summary of structural information of porous Co_3O_4 nanostructure and their OER electrocatalytic activities in 0.1 M KOH[a]

Sample	BET (m²/g)	Pore Size (nm)[b]	Pore Density[c]	Particles size (nm)	η [d] @ 5mA/cm²	η @ 0mA/cm²	η @ 20mA/cm²	J[e] @ 1.0 V vs. Ag/AgCl (3M)	TOF (s⁻¹) @ η=400mV
ITO	-	-	-	-	-	-	-	0.86	-
Co(OH)₂	68.3	-	-	-	587	665	-	15.1	5.56×10^{-5}
Co₃O₄-250	160.9	3.0	200	3~4	472	523	591	47.9	2.81×10^{-3}
Co₃O₄-300	138.0	4.0	80	7~10	509	567	650	34.5	7.41×10^{-4}
Co₃O₄-400	106.9	3~8	40	11~20	535	593	666	33.4	5.25×10^{-4}
Co₃O₄-500	87.6	5~15	25	13~24	539	606	692	26.4	5.61×10^{-4}
Co₃O₄-Meso	128.1	6.5[f]	-	8~12	596	652	734	20.1	4.01×10^{-4}
Ir/C	-	-	-	-	662	709	-	13.6	-

[a] Current density in unit of mA/cm² and overpotential in unit of mV;[b] Pore size was obtained from TEM analysis except Co₃O₄-Meso; [c] Pore density is the estimated number of pores in a square of 100×100 nm² over 50 nanoplates, which was calculated ratio of number of pores on each nanoplate/geometrical area of the nanoplate. [d] η refers to the overpotential in unit of mV. [e] refers to the current density at unit of mA/cm². [f] Obtain from BET analysis.

(Fig. 2a-2d). The generation of pores confined within thenanoplates could be attributed to the slow dehydration, in which the loss of water molecules created the pores without disturbing the plate shape. The structural information of all products is summarized in Table 1. Co₃O₄-250 has the largest surface area of 160.9 m²/g, which is much larger than 68.3 m²/g of β-Co(OH)₂ nanoplates and comparable to mesoporous Co₃O₄ synthesized by nanocasting method.[34] The average pore size (3.7 nm) of Co₃O₄-250 derived from BET measurement (Fig. S4) is well consistent with ~3.0 nm as observed in TEM image (Fig. 2a, Fig. S5). With the increased annealing temperature, the surface areas of the porous Co₃O₄ nanoplates decreased to 138.0, 106.9 and 87.6 m²/g for Co₃O₄-300, Co₃O₄-400 and Co₃O₄-500, respectively. Meanwhile, increasing the calcination temperature, the average number of the pores for 100 × 100 nm² was significantly reduced from 200 to 80, 40 and 25 for Co₃O₄-250, Co₃O₄-300, Co₃O₄-400 and Co₃O₄-500, respectively. And also the pore size became large due to the structural collapse under high temperature treatment. As shown in Table 1 and evidenced in Fig. 2, the large pores over 10 nm were observed in Co₃O₄-500.

Electrocatalytic water oxidation

To evaluate the OER activities of the porous Co₃O₄ nanoplates, the catalysts were loaded onto an ITO electrode with a density of 0.56 mg/cm² for catalytic active components by drop casting. The thermodynamic potentials for the electrodes, $E^o_{OH^-/O2}$ = 0.324 V *vs.* Ag/AgCl at pH=12, 0.265 V *vs.* Ag/AgCl at pH=13, and 0.206 V *vs.* Ag/AgCl at pH=14,[16, 34] were used for all overpotential measurements in 0.01, 0.1 and 1.0 M KOH electrolyte solutions, respectively. The LSV curves of a bare ITO substrate, commercial 10 wt% Ir/C, β-Co(OH)₂ nanoplate, and porous Co₃O₄-250, Co₃O₄-300, Co₃O₄-400 and Co₃O₄-500 nanoplate electrodes in 0.1 M KOH are given in Fig. 3a. Compared to the strong catalytic currents of catalyst loaded electrodes, a very weak current density (0.86 mA/cm²) of the bare ITO substrate at 1.0 V applied potential (vs. Ag/AgCl) indicates the inactive nature of ITO towards the O₂ evolution

and a background correction for ITO support is unnecessary for all catalytic electrodes.

The electrocatalytic activities of all catalysts in 0.1 M KOH including the overpotentials at the specified current densities of 5 or 10 or 20 mA/cm², the current densities at 1.0 V (vs. Ag/AgCl) and the calculated turnover frequencies (TOFs) at 400 mV overpotential, are summarized in Table 1. The best activity was observed on the electrode loaded with Co₃O₄-250. As given in Fig. 3a, the onset potential of the Co₃O₄-250 is 0.55 V vs Ag/AgCl, which is 110, 125, 125 and 140 mV ahead of the Co₃O₄-300, Co₃O₄-400, Co₃O₄-500 and the Co(OH)₂ electrode, respectively. At a current density of 5 mA/cm², the overpotential for Co₃O₄-250 is 472 mV while the overpotentials for Co₃O₄-300, Co₃O₄-400 and Co₃O₄-500 are 509, 535 and 539 mV, respectively. A similar trend was also observed at the current densities of 10 and 20 mA/cm². The current density of 47.9 mA/cm² for the Co₃O₄-250 electrode at 1.0 V (vs. Ag/AgCl) was much larger than those of 34.5, 33.4 and 26.4 mA/cm⁻² for the Co₃O₄-300, Co₃O₄-400 and Co₃O₄-500 electrodes, respectively.

The electrocatalytic OER activity of β-Co(OH)₂ nanoplates was also measured. The overpotentials at current densities of 5 and 10 mA/cm² were respectively 587 and 665 mV, much larger than those of porous Co₃O₄ nanoplates (Table 1). The current density at 1.0 V (*vs.* Ag/AgCl) was 15.1 mA/cm², which was 31.5 % and 57.2% of the current densities of the Co₃O₄-250 and Co₃O₄-500 electrodes, respectively. The results suggest that the porous Co₃O₄ nanoplates deliver much better OER activity than that of the Co(OH)₂ nanoplates.

It is difficult to directly compare the electrocatalytic activities of the porous Co₃O₄ nanoplates with previously reported Co₃O₄ catalysts since many factors affect OER, such as material synthesis methods, catalysts loading, supports, pH value of electrolyte solution, *et.al.*.[16] Herein, ordered mesoporous Co₃O₄, named as Co₃O₄-Meso, was prepared by using KIT-6 mesoporous silica as the hard template at 35 °C, which exhibited the largest surface area and the best OER activity in a previous report.[34] The ordered mesoporous Co₃O₄
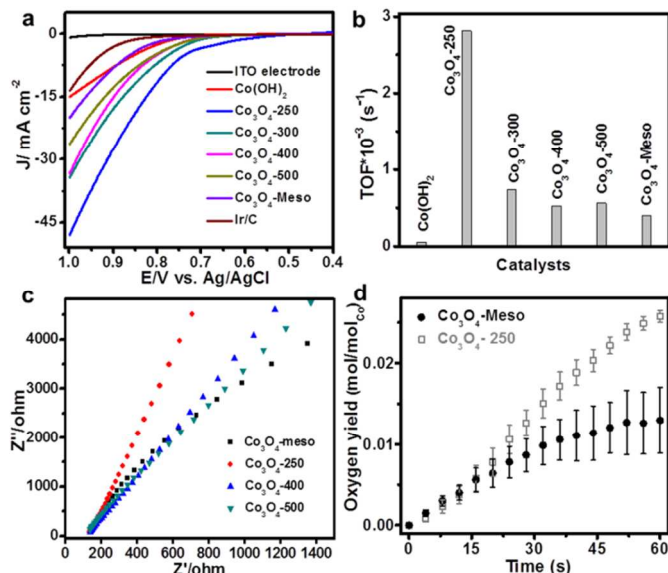
Fig. 3 Electrochemical performance of catalysts loaded on ITO electrodes. (a) Linear sweep voltammograms of all catalytic electrodes in 0.1 M KOH. (b) Calculated TOFs for all catalysts in 0.1 M KOH. (c) Impedance Nyquist plots of the nanoporous Co_3O_4-250, Co_3O_4-300, Co_3O_4-400 and Co_3O_4-Meso electrodes. (d) Photocatalytic oxygen yield from $[Ru(bpy)_3]^{2+}$-persulfate system for Co_3O_4-250 and Co_3O_4-Meso.

Fig. 4 (a) Linear voltammograms of Co_3O_4-250 in 0.01 M, 0.1 M and 1.0 M KOH without iR correction. (b) Plot of overpotentials of Co_3O_4-250 vs. specific current densities of 5, 10, 20 mA/cm^2 in 0.01 M, 0.1 M and 1.0 M KOH. In 0.01 M KOH, the current densities of 10 and 20 mA/cm^2 for Co_3O_4-250 electrode were not observed under the applied potentials of 0.4-1.0 V (vs. Ag/AgCl). (c) Electrochemical performance of Co_3O_4-250, Co_3O_4-Meso and commercial 10 wt% Ir/C after 95% iR corrections in 1.0 M KOH. (d) Tafel plots of Co_3O_4-250 and Co_3O_4-Meso catalysts loaded on ITO recorded in 1.0 M KOH.

(Fig. S6) has a surface area of 128.1 m^2/g. The electrocatalytic activity of Co_3O_4-Meso was also evaluated as a comparison. The overpotentials for 5, 10, 20 mA/cm^2 current densities were respectively 596, 652 and 734 mV, which were much larger than the porous Co_3O_4 nanoplates at the corresponded current densities. The current density of 20.1 mA/cm^2 at 1.0 V (vs. Ag/AgCl) for Co_3O_4-Meso was 6.3 mA/cm^2 smaller than that of Co_3O_4-500 and only 42% of Co_3O_4-250. The commercially available 10 wt% Ir/C catalyst was also measured side by side. The onset potential of Ir/C catalyst was similar to that of porous Co_3O_4 catalysts, but its OER current density far fell below those of porous Co_3O_4 nanoplates (Fig. 3a). The current density at 1.0 V (vs. Ag/AgCl) was 13.6 mA/cm^2, only 28.4% of that for Co_3O_4-250. These results demonstrate that our approach can achieve highly active porous Co_3O_4 catalysts for OER.

Assuming that Faraday efficiency is 100 % and every surface cobalt atom is an active site for OER, the TOF for each catalyst can be calculated from the electrode current density at an overpotential of 400 mV. The calculated TOF for Co_3O_4-250 in 0.1 M KOH was 2.81×10^{-3} s^{-1}, which was 3.80, 5.35 and 5.01 times higher than those for Co_3O_4-300, Co_3O_4-400 and Co_3O_4-500 (Fig. 3b), respectively. The highest TOF and the lowest overpotentials at a specific current density (Table 1) for Co_3O_4-250 unambiguously illustrate the importance of specific physicochemical properties of Co_3O_4 catalysts for OER.

As summarized in Table 1, the surface area of Co_3O_4-250 (160.9 m^2/g) is only 1.16 ~ 1.84 times larger than those of Co_3O_4 catalysts, while the TOF of Co_3O_4-250 is 3.80 ~ 5.35 times higher than those of Co_3O_4 catalysts. Hence, surface area cannot afford the explanation of OER activities in this work. Ideally, the surface activity of cobalt-based active sites should be equal for all catalysts if they are under the same reactive

environmental, leading to the same values of TOFs for all Co_3O_4 catalysts. Such a high TOF for Co_3O_4-250 can be partly attributed to the high pore density and the small crystalline size of nanowalls of Co_3O_4-250, which both provide more corner and edge sites. It is well known that the catalytic active atoms at corner or edge sites of a catalyst with a lower coordination number always exhibit a higher catalytic activity. This phenomenon becomes significant for nanoscale catalysts, which was neglected in previous studies on the surface area effect of Co_3O_4 nanoparticles on OER.[16]

Herein, the crystalline size of Co_3O_4-250 (Fig. 2a) is around 3.0 nm, which is much smaller than those of other porous Co_3O_4 nanoplates (Fig. 2) and 6.5 nm of Co_3O_4-Meso (Fig. S6). The amount of the corner and edge cobalt atoms of Co_3O_4-250 is much larger than that of other Co_3O_4 catalysts. Therefore, a higher activity of Co_3O_4-250 for water oxidation was expected and indeed observed.

Although the surface areas of Co_3O_4-400 and Co_3O_4-500 are smaller than that of Co_3O_4-Meso and their crystalline sizes are larger than that of Co_3O_4-Meso, the calculated TOFs are still near 1.5 times higher than that of Co_3O_4-Meso. This result might be explained by the diffusion of electrolyte and the transport of the generated O_2. The O_2 regeneration on each active site could only happen after the escape of the produced O_2. The channel length of the Co_3O_4-Meso catalysts is usually over hundreds of nanometer, with a much longer pathway for the escape of the generated O_2 and the diffusion of the electrolyte. In contrast, porous Co_3O_4 nanoplates with a 10 nm thickness may provide a much shorter channel length. The diffusion of electrolyte or the generated oxygen can be evaluated using Nyquist plots obtained from EIS (Fig. 3c). In
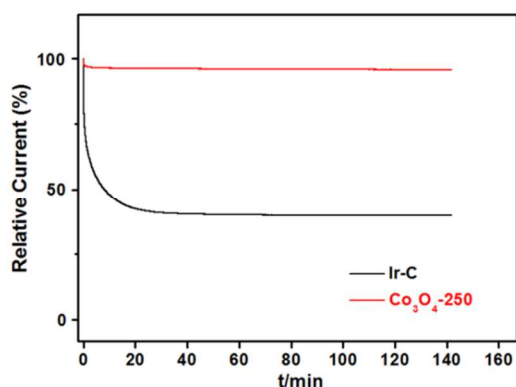
Fig. 5 Chronoamperometric measurements of Co_3O_4-250 and commercially available 10wt % Ir/C catalysts biased at 0.8 V (vs. Ag/AgCl) for 140 min in 0.1 M KOH.

the low frequency ranges of the Nyquist plots, the straight line corresponds to the Warburg resistance relative to the diffusion of the electrolyte within the electroactive materials. Generally, the higher slope indicates more efficient diffusion of the electrolyte. [41, 42] The slopes of the Nyquist plots are 82.8°, 77.5° and 74.5° for Co_3O_4-250, Co_3O_4-400 and Co_3O_4-500 electrodes, which are much larger than that of Co_3O_4-Meso (69.0°). Therefore, the much more efficient diffusion of electrolyte for porous Co_3O_4 nanoplate electrodes can help the escape of the generated O_2 and hence improve the OER activity of the porous Co_3O_4 nanoplates.

The iR-correction (Fig. S7) was also performed to further evaluate the activities of the catalysts. Fig. S7 shows the 95% iR-corrected polarization curves of the Co_3O_4-250, Co_3O_4-Meso and Ir/C catalysts on ITO electrodes in 0.1 M KOH. The measured current density of the Co_3O_4-250 electrode at 1.0 V (vs. Ag/AgCl) was 140.0 mA/cm^2, which was 4.67 and 8.92 times higher than those for the Co_3O_4-Meso and Ir/C electrodes, respectively. To the thermodynamic side, the overpotentials for the Co_3O_4-250, Co_3O_4-Meso and Ir/C catalysts at 10 mA/cm^2 current density were 490, 634, and 700 mV, respectively. The results also confirm that Co_3O_4-250 with the largest surface area, the smallest crystalline size and the shortest pore length has the best activity for water oxidation, compared to ordered mesoporous Co_3O_4 and commercially available Ir/C catalysts.

Photocatalytic water oxidation

To further confirm oxygen evolution activities, the photocatalytic activities of porous Co_3O_4-250 and Co_3O_4-Meso were also evaluated in a $[Ru(bpy)_3]^{2+}$-persulfate system, in which $[Ru(bpy)_3]^{2+}$ acts as the light sensitizer and persulfate functions as sacrificial electron acceptor. [19, 23, 40] The catalytic performance of the two catalysts was measured in a typical Clark electrode system. In Fig. 3d, the porous Co_3O_4-250 catalysts exhibited a higher activity for oxygen evolution than the Co_3O_4-Meso catalysts. The calculated TOF of 4.2×10^{-4} s^{-1} per Co atom or $\sim 3.2 \times 10^{-3}$ s^{-1} per surface Co atom for the Co_3O_4-250 catalysts is higher than the TOF (2.1×10^{-4} s^{-1} per Co atom) of Co_3O_4-Meso and the TOFs ($2.0 \sim 4.02 \times 10^{-4}$ s^{-1} per Co atom) reported for mesoporous Co_3O_4 and Co_3O_4

nanoclusters supported in mesoporous silica. [19, 23, 40] The results further indicate that the porous Co_3O_4 nanoplates display a feature of the high OER activity for the photocatalytic water splitting reaction.

Effect of the electrolyte basicity on the catalytic activity of Co_3O_4

The concentration of electrolyte also significantly affects the activity of Co_3O_4 nanostructures for water oxidation. The catalytic behaviors of all catalysts were also evaluated under the 0.01 and 1.0 M KOH solutions. As shown in Fig. 4 and Fig. S8, the catalytic performance of the catalysts in 0.01 M and 1.0 M KOH was very similar to those in 0.1 M KOH, in which Co_3O_4-250 showed the highest OER activities. Plots of electrocatalytic activities of Co_3O_4-250 vs. potential in various concentrations of KOH are presented in Fig. 4a. A low current density of 5.43 mA/cm^2 at 1.0 V (vs. Ag/AgCl) is observed for Co_3O_4-250 in 0.01 M KOH. Increasing the concentration of KOH to 0.1 M and 1.0 M gives a much higher current density of 47.9 and 220.7 mA/cm^2, respectively. As shown in Fig. 4b, the overpotentials of 720, 472 and 414 mV were recorded at 5 mA/cm^2 current density for 0.01 M, 0.1 M and 1.0 M KOH, respectively. The observation is very consistent with previous report that raising the concentration of OH$^-$ in the electrolyte can increase the OER activity of Co_3O_4 catalysts. [34]

Fig. 4c presents the electrocatalytic activities (with iR correction) of Co_3O_4-250, Co_3O_4-Meso and commercially available Ir/C catalysts in 1.0 M KOH electrolyte solution. Similar to the results of electrochemical performance of three catalysts in 0.1 M KOH, Co_3O_4-250 catalysts displayed the best activity, in terms of the highest current densities at the specific applied bias and the lowest overpotentials at the specific current densities. We also fitted the polarization curves of Co_3O_4-250 and Co_3O_4-Meso shown in Fig. 4c to the Tafel equation. As presented in Fig. 4d, the derived Tafel slopes for Co_3O_4-250 and Co_3O_4-Meso are 71 and 98 mV/dec, respectively. Considering the difference in their crystalline sizes, the lower value of Tafel slope for Co_3O_4-250 may be attributed to the smaller crystalline size by providing the abundant amount of the active surface sites with low coordination numbers, compared that of Co_3O_4-Meso. The value of the Tafel slope of Co_3O_4-250 is close to that reported for the reduced porous Co_3O_4 nanorwires (72 mV/dec), [43] Co_3O_4 nanoparticles (78 mV/dec) and Co_3O_4/graphene composites (68 mV/dec), [36] suggesting a high OER activity of the porous Co_3O_4 nanoplates.

Catalytic stability of Co_3O_4-250

Besides the catalytic activity, material stability is another major concern to design cost-effective OER catalysts. The stability of Co_3O_4-250 by running chronoamperometric responses (i-t) at 0.8 V (vs. Ag/AgCl) in 0.1 M KOH was performed. During the measurements, the working electrode was continuously rotating at 1600 rpm to remove the generated O_2 bubbles. As given in Fig. 5, the stabilized current density indicates no obvious deactivation of Co_3O_4-250 over 140 min, while an apparent dropped current density for commercially available Ir/C was

recorded at the initial period. The results suggest that the Co$_3$O$_4$-250 exhibits a good catalytic stability under the strong alkaline conditions, despite its nature of high surface area and nanoscale crystalline size.

Conclusions

In summary, we have reported a new type of ultrathin porous Co$_3$O$_4$ nanoplates, involving the synthesis of β-Co(OH)$_2$ nanoplates as precursor structures and subsequent high temperature treatment in air. The pore size, pore density and crystalline size of the nanowalls can be easily tunable by the annealing temperatures. Performing the catalytic reaction under the same conditions, the highest catalytic activity was achieved with Co$_3$O$_4$-250, which has the largest surface area, the smallest crystalline size, the shortest oxygen escape length, and the most efficient electrolyte diffusion within the electrodes. Hence, Co$_3$O$_4$-250 catalysts provide more surface catalytic sites and more corner and edge sites with high catalytic activity and ensure the efficient charge and chemical transfer due to the structural features. Combining all together, Co$_3$O$_4$-250 catalysts exhibit a high catalytic activity (reflected by the values of TOFs and Tafel slope). The excellent electrochemical stability of Co$_3$O$_4$-250 catalysts was also demonstrated.

Acknowledgements

Notes and references

^{a} Center of Applied Chemical Research, Frontier Institute of Science and Technology, Xi'an Jiaotong University, Xi'an, China 710049. E-mail: yongquan@mail.xjtu.edu.cn; yyma@mail.xjtu.edu.cn
^{b} State Key Laboratory for Mechanical Behavior of Materials, Xi'an Jiaotong University, Xi'an, 710049, China

† Footnotes should appear here. These might include comments relevant to but not central to the matter under discussion, limited experimental and spectral data, and crystallographic data.
Electronic Supplementary Information (ESI) available: [SEM images of vertically aligned β-Co(OH)$_2$ nanoplates; TEM images for β-Co(OH)$_2$ nanoplates annealed at 600 °C and ordered mesoporous Co$_3$O$_4$; BET spectrum for Co$_3$O$_4$-250; Electrochemical performance of three catalysts after 90% and 95% iR corrections in 0.1 M KOH solution; Electrochemical performance of catalysts in 0.01 M and 1.0 M KOH electrolyte solution; and Photocatalytic activities of Co$_3$O$_4$-250 and Co$_3$O$_4$-Meso for oxygen evolution in a [Ru(bpy)$_3$]$^{2+}$-persulfate system; and TOF calculation.]. See DOI: 10.1039/b000000x/

1. M. W. Kanan, Y. Surendranath and D. G. Nocera, *Chem. Soc. Rev.* 2009, **38**, 109-114

2. D. G. Nocera, *Acc. Chem. Res.* 2012, **45**, 767-776

3. H. L. Wang and H. J. Dai, *Chem. Soc. Rev.* 2013, **42**, 3088-3113.

4. Y. Qu and X. Duan, *Chem. Soc. Rev.* 2013, **42**, 2568-2580.

5. Y. Qu and X. Duan, *J. Mater. Chem.* 2012, **22**, 16171-16181.

6. Y. Li and J. Z. Zhang *Laser Photonics Rev.* 2010, **4**, 517-528.

7. G. M. Wang, H. Y. Wang, Y. C. Ling, Y. C. Tang, X. Y. Yang, R. C. Fitzmorris, C. C. Wang, J. Z. Zhang and Y. Li, *Nano Lett.* 2011, **11**, 3026-3033.

8. Y. Liang, Y. Li, H. Wang and H. J. Dai, *J. Am. Chem. Soc.* 2013, **135**, 2013-2036.

9. T. Nakagawa, N. S. Bjorge and R. W. Murray, *J. Am. Chem. Soc.* 2009, **131**, 15578-15579

10. S. W. Gersten, G. J. Samuels and T. J. Meyer, *J. Am. Chem. Soc.* 1982, **104**, 4029-4030.

11. G. Beni, L. M. Schiavone, J. L. Shay, W. C. Dautremont and B. S. Schneider, *Nature* 1979, **282**, 281-283.

12. H. Over *Chem. Rev.* 2012, **112**, 3356-3426

13. F. Jiao and H. Frei, *Energy Environ. Sci.* 2010, **3**, 1018-1027.

14. K. N. Ferreira, T. M. Iverson, K. Maghlaoui, J. Barber and S. Iwata, *Science* 2004, **303**, 1831-1838.

15. G. P. Gardner, Y. B. Go, D. M. Robinson, P. F. Smith, J. Hadermann, A. Abakumov, M. Greenblatt and G. C. Dismukes, *Angew. Chem. Int. Ed.* 2012, **51**, 1616-1619.

16. A. J. Esswein, M. J. McMurdo, P. N. Ross, A. T. Bell and T. D. Tilley, *J. Phys. Chem. C* 2009, **113**, 15068-15072.

17. S. Cobo, J. Heidkamp, P. A. Jacques, J. Fize, V. Fourmond, L. Guetaz, B. Jousselme, V. Ivanova, H. Dau, S. Palacin, M. Fontecave and V. Artero, *Nat. Mater.* 2012, **11**, 802-807.

18. C. A. Kent, J. J. Concepcion, C. J. Dares, D. A. Torelli, A. J. Rieth, A. S. Miller, P. G. Hoertz and T. J. Meyer, *J. Am. Chem. Soc.* 2013, **135**, 8432-8435

19. F. Jiao and H. Frei, *Angew. Chem. Int. Ed.* 2009, **48**, 1841-1844.

20. M. W. Kanan and D. G. Nocera, *Science* 2008, **321**, 1072-1075.

21. T. L. Wee, B. D. Sherman, D. Gust, A. L. Moore, T. A. Moore, Y. Liu and J. C. Scaiano, *J. Am. Chem. Soc.* 2011, **133**, 16742-16745.

22. R. Subbaraman, D. Tripkovic, K. C. Chang, D. Strmcnik, A. P. Paulikas, P. Hirunsit, M. Chan, J. Greeley, V. Stamenkovic and N. M. Markovic, *Nat. Mater.* 2012, **11**, 550-557.

23. J. Rosen, G. S. Hutchings and F. Jiao, *J. Am. Chem. Soc.* 2013, **135**, 4516-4521.

24. X. M. Zhou, Z. M. Xia, Z. Y. Zhang, Y. Ma and Y. Qu, *J. Mater. Chem. A*, 2014, **2**, 11799-11806.

25. I. M. Sadiek, A. M. Mohammad, M. E. El-Shakre and M. S. El-Deab, *Int. J. Hydrogen Energy* 2012, **37**, 68-77.

26. M. Gong, Y. G. Li, H. L. Wang, Y. Y. Liang, J. Z. Wu, J. G. Zhou, J. Wang, T. Regier, F. Wei and H. J. Dai, *J. Am. Chem. Soc.* 2013, **135**, 8452-8455.

27. D. K. Zhong, J. W. Sun, H. Inumaru and D. R. Gamelin, *J. Am. Chem. Soc.* 2009, **131**, 6086-6087.

28. N. T. Hahn, H. Ye, D.W. Flaherty, A. J. Bard and C. B. Mullins, *ACS Nano* 2010, **4**, 1977-1986.

29. T. Takashima, K. Hashimoto and R. Nakamura, *J. Am. Chem. Soc.* 2012, **134**, 18153-18156.

30. Y. Gorlin, B. Lassalle-Kaiser, J. D. Benck, S. Gul, S. M. Webb, V. K. Yachandra, J. Yano and T. F. Jaramillo, *J. Am. Chem. Soc.* 2013, **135**, 8525-8534.

31. M. W. Kanan, J. Yano, Y.Surendranath, M.Dincă, V. K.Yachandra and D. G. Nocera, *J. Am. Chem. Soc.* 2010, **132**, 13692-13701.

32. N. S. McCool, D. M. Robinson, J. E. Sheats and G. C. Dismukes, *J. Am. Chem. Soc.* 2011, **133**, 11446-11449.

33. L. P. Wang and T. V.Voorhis, *J. Phys. Chem. Lett.* 2011, **2**, 2200-2204.

34. H. Tüysüz, Y. J. Hwang, S. B. Khan, A. M. Asiri and P. D. Yang, *Nano Res.* 2012, **6**, 47-54.

35. J. Wu, Y. Xue, X. Yan, W. S. Yan, Q. M. Cheng and Y. Xie, *Nano Res.* 2012, **5**, 521-530.

36. Y. Y. Liang, Y. G. Li, H. L. Wang, J. G. Zhou, J. Wang, T. Regier and H. J. Dai, *Nat. Mater.* 2011, **10**, 780-786.

37. X. M. Ni, H. G. Zheng, X. K. Xiao, X. Jin and G. G. Liao, *J. Alloys Compd.* 2009, **484**, 467-471.

38. J. Yang, H. W. Liu, W. N. Martens and R. L. Frost, *J. Phys. Chem. C* 2010, **114**, 111-119.

39. M. C. Biesingera, B. P. Paynec, A. P. Grosvenord, L. W.M. Laua, A. R. Gersonb and R. St. C. Smart, Appl. Surf. Sci. 2011, 257, 2717-2730.

40. S. Yusuf and F. Jiao, *ACS Catal.* 2012, **2**, 2753-2760.

41. Y. H. Xiao, S. J. Liu, F. Li, A. Q. Zhang, J. H. Zhao, S. M. Fang and D. Z. Jia, *Adv. Funct. Mater.*, 2012, **22**, 4052.

42. Y. H. Xiao, A. Q. Zhang, S. J. Liu, J. H. Zhao, S.M. Fang, D. Z. Jia and F. Li, *J. Power Sources*, 2012, **219**,140-146.

43. Y. C. Wang, T. Zhou, K. Jiang, P. M. Da, Z. Peng, J. Tang, B. Kong,W. B. Cai, Z. Q. Yang and G. F. Zheng, *Adv. Energy Mater.*, 2014, DOI: 10.1002/aenm.201400696.

Journal of Materials Chemistry A Accepted Manuscript